Agricultural and Forest Meteorology 327 (2022) 109222

Contents lists available at ScienceDirect

Agricultural and Forest Meteorology

journal homepage: www.elsevier.com/locate/agrformet

Quantifying the impacts of DEM uncertainty on clear-sky surface shortwave radiation estimation in typical mountainous areas

Yichuan Ma [a], Tao He [a,*], Shunlin Liang [b], Xiongxin Xiao [a]

[a] School of Remote Sensing and Information Engineering, Wuhan University, Wuhan 430079, China
[b] Department of Geography, University of Hong Kong, Hong Kong 999077, China

ARTICLE INFO

Keywords:
Mountain
Downward shortwave radiation
Net shortwave radiation
Clear-sky shortwave radiation
Digital elevation model (DEM)
Uncertainty analysis

ABSTRACT

Accurate estimation of shortwave radiation in mountains will advance our knowledge of climate change effects, especially on mountain ecosystems. Recently, some approaches have been developed to estimate shortwave radiation parameters in mountains with satellite data, but few attempts were made to understand the impacts of digital elevation model (DEM) uncertainty on estimates. Our study investigates such impacts quantitatively in clear-sky conditions at multiple spatial and temporal scales (30–3000 m, instantaneous to daily). We employed a retrieval algorithm to estimate instantaneous and daily mean clear-sky downward shortwave radiation (DSR) and net shortwave radiation (NSR), as a proxy for our evaluation. The accuracy of our method based on accurate terrain data was verified against in-situ measurements with root-mean-square errors (RMSEs) of 65.9 W/m^2 and 65.1 W/m^2 for instantaneous DSR and NSR, and 21.2 W/m^2 and 22.5 W/m^2 for daily mean values, respectively. When using satellite DEM products, the DSR estimation uncertainty could increase by 64.0% for instantaneous values and 46.2% for daily mean values. Using AW3D30 and SRTM DEMs for DSR estimation led to a maximum difference of 16.8% (103.6 W/m^2) and 13.0% (25.8W/m^2) on instantaneous and daily mean values, respectively. That estimation difference of shortwave radiation decreased with an increase in spatial scale, with RMS deviation lower than 2% for spatial resolution beyond 3000 m. In addition, the evaluation of introducing random errors into AW3D30 DEM showed that the shortwave radiation uncertainty caused by DEM may exceed the algorithm uncertainty itself with DEM mean absolute error (MAE) equaling about 5.0 m. Considering the current DEM accuracy, the impacts of DEM errors on shortwave radiation in mountains cannot be ignored. This study emphasizes the potential impacts of DEM uncertainty on surface shortwave radiation estimation, which is crucial in using satellite-derived datasets for energy balance calculation and climate change applications in mountains.

1. Introduction

Shortwave radiation, including downward shortwave radiation (DSR) and net shortwave radiation (NSR), profoundly influences the land surface radiation budget and is the dominant energy for clean energy production and ecosystem productivity (Liang et al., 2019), wherein NSR = DSR × (1-albedo) (albedo is defined as the ratio of upward shortwave radiation and DSR). Accurate estimation of shortwave radiation is essential for monitoring and evaluating global environment (Huang et al., 2016), solar energy utilization (Xu et al., 2021), ecosystem (Chen et al., 2021; Wu et al., 2021), and global energy balance (Wild et al., 2013; Zapadka et al., 2020). Mountains cover around a quarter of the land surface on Earth (Blyth et al., 2002). Under the background of global climate change, the mountain ecosystem is especially fragile, and now is undergoing considerable changes (Immerzeel et al., 2020), such as elevation-dependent warming (Pepin et al., 2015), glacier melt (Li et al., 2021), and plant communities transformation (Gottfried et al., 2012). In mountains, spatial and temporal heterogeneity of shortwave radiation determines local variation and dynamics of energy budget, vegetation, and hydrology, such as snowmelt, evaporation, vegetation phenology, and surface warming (Garen and Marks, 2005; He et al., 2018b; Nyman et al., 2018; Xiao et al., 2020; Xie and Li, 2020; Xu et al., 2020; Zhao et al., 2021). Therefore, the high-accuracy estimation of DSR and NSR in mountains helps in understanding numerous land processes and climate change.

To date, numerous methods have been proposed to derive DSR and NSR for open areas (Carmona et al., 2015; Chen et al., 2022; He et al., 2015; Huang et al., 2019; Wang et al., 2021). In mountains, however,

* Corresponding author: Wuhan University, China.
E-mail address: taohers@whu.edu.cn (T. He).

https://doi.org/10.1016/j.agrformet.2022.109222
Received 3 March 2022; Received in revised form 19 September 2022; Accepted 17 October 2022
Available online 29 October 2022

ignoring topographic effects would have a considerable impact on shortwave radiation calculation (Chen et al., 2006; Lai et al., 2010). For example, Lee et al. (2013) reported Tibetan Plateau would receive more DSR by about 14W/m^2 when considering 3D mountain structure using a 1-km digital elevation model (DEM); and Wang et al. (2018) reported the error could exceed 600W/m^2 when neglecting topographic effects for DSR at a Moderate Resolution Imaging Spectroradiometer (MODIS) pixel scale, and a similar error in magnitude for NSR using Advanced Spaceborne Thermal Emission and Reflection Radiometer (ASTER) Global Digital Elevation Model (GDEM). Hao et al. (2021) reported the absolute differences in NSR simulation between sub-grid topographic and plane-parallel schemes could reach 20W/m^2 in Tibetan Plateau using the 90 m Shuttle Radar Topography Mission (SRTM) DEM.

Nowadays, some researchers have proposed clear-sky shortwave radiation estimation algorithms in mountains. Most of them separately estimated DSR and surface albedo to calculate NSR in mountains. Mountain radiative transfer process (Sandmeier and Itten, 1997) was always used for DSR characterization, composed of direct radiation, diffuse radiation, and reflected radiation from surrounding environments. With this physical theory, some studies derived DSR in mountains (Aguilar et al., 2010; Zhang et al., 2015). With DSR estimations arising from the above theory, Hansen et al. (2002), Amatya et al. (2015), and Chen et al. (2013) calculated albedo using narrowband-to-broadband conversions (Liang, 2001) and finally obtained instantaneous NSR. Long et al. (2010) derived the 500 m daily average NSR by combing estimated DSR and MCD43A1 albedo products. However, they seldom considered topographic effects in surface albedo (Hao et al., 2019a; Ma et al., 2022; Wen et al., 2022; Wu et al., 2018), leading to errors in shortwave radiation estimation. Meanwhile, the instantaneous observations from satellite overpass time cannot represent the average shortwave radiation in a day (Chen et al., 2022); Yan et al. (2018) declared that the current temporal extrapolation methods, such as the sinusoidal model (Bisht et al., 2005), would lead to 60W /m^2 errors for daily mean DSR estimation in mountains.

Topographic parameters derived from DEM (e.g., slope and aspect) are key to describing surface radiation in mountains (Dozier and Frew, 1990; Sandmeier and Itten, 1997). Thus, DEM is the basic and critical input data for mountainous shortwave radiation estimation models. Past studies used different DEMs, e.g., ASTER GDEM, SRTM DEM, and Advanced Land Observing Satellite "ALOS" World 3D 30m (AW3D30) DEM, at different spatial resolutions (e.g., 1 arc-second and 3 arc-second). All of these DEMs are now available at 1 arc-second (30 m) spatial resolution, but the acquisition time, the generation techniques (Guth et al., 2021), and data accuracy (Carrera-Hernández, 2021) are different. The errors and differences in DEM data can be propagated into topographic parameters calculation and then cased the deviations of shortwave radiation in mountainous areas (Wang and Wang, 2015).

There are some primary findings in the influences of DEM on shortwave radiation estimation over mountainous areas. Huang et al. (2017) reported that the 30 m DEM provided better performance than the 90 m DEM in terms of DSR estimation on sloping terrain, where the root mean squared errors (RMSEs) were 58.05W/m^2 and 78.36W /m^2 against in-situ measurements, respectively. Olson et al. (2019) also found that the bias in the modeled shortwave radiation increased as the DEM resolution downsampled (from 8 m to 30 m). Hao et al. (2019b) explored how the geolocation uncertainty of DEM impacted the DSR estimations in mountains using simulation data and found 600W /m^2 deviations when the geolocation bias of DEM was lower than half a pixel. Wang and Wang (2015) compared solar radiation estimation results using six different DEM datasets and declared that although the six DEM datasets were in good agreement with each other (i.e., linear correlation coefficients higher than 0.98), the solar radiation results considerably differed, where correlation coefficients could be lower than 0.5. In general, the accuracy of input DEM has serious implications on shortwave radiation results. However, (i) how large deviations could be introduced by using different DEM products, and (ii) whether it could strongly impact shortwave radiation mappings in mountains are still unknown. Meanwhile, quantitative evaluation of shortwave radiation uncertainty caused by DEM errors at different spatial and temporal scales remains a void, hindering a better understanding of possible issues in mountainous applications.

The objective of this paper is to comprehensively quantify the impacts of DEM uncertainty on shortwave radiation estimation in mountains. We implemented the evaluation using an instantaneous and daily mean DSR and NSR estimation method as a proxy, where the main idea to consider topography was the same as other shortwave radiation estimation algorithms, demonstrating our study's universal applicability to mountainous shortwave radiation estimation and modeling fields. We adopted the evaluation and quantification using in-situ measured topographic information, DEM datasets, and simulated data: (i) We evaluated the estimation accuracy based on in-situ measured topographic information and topographic factors derived from DEM datasets, respectively; (ii) We compared the estimated shortwave radiation using different DEMs at diverse spatial and temporal scales; (iii) We evaluated how large shortwave radiation uncertainty could be caused by introducing random errors into AW3D30 DEM. The materials and methods are presented in Sections 2 and 3, respectively. The results are shown in Section 4 and discussed in Section 5. Finally, the conclusions are provided in Section 6.

2. Materials

2.1. In-situ measurements

There are some ground flux stations in mountainous areas over the globe; however, most of them are set in the horizontal direction, which cannot measure the radiation reaching or reflected from the sloping terrains exactly. We collected valuable slope-parallel measured shortwave flux (Wu et al., 2018) with various slopes and aspects from Chengde, China, as shown in Table 1. All in-situ measured shortwave radiation data are from four-component radiometer CNR4 and EKO MR-60 which measured upward and downward shortwave radiation from 300 nm to 2800 nm. The in-situ measured shortwave radiation data have been checked and used in previous studies (Ma et al., 2022; Wang et al., 2018). We excluded outliers (following https://www.soda-pro.com/help/general/quality-check, last accessed 10/Jul/2022) and cloud-contaminated data for validation and analysis. The slopes and aspects are measured by a level meter and electronic compass.

2.2. Landsat data

Landsat satellite series have provided global land observations for over 40 years, with data freely available from the United States

Table 1
Information of in-situ measurements for validation.

Site name	Latitude/ Longitude(°)	Slope/ Aspect(°)	Years	References
Chengde-1	42.3974N/ 117.3992E	11.0/ 79.8	2018–2020	Yan et al. (2018), Yan et al. (2021), Chu et al. (2019)
Chengde-2	42.3968N/ 117.3979E	16.3/ 266.5	2018–2020	
Chengde-3	42.3927N/ 117.3973E	27.5/ 217.5	2018–2020	
Chengde-4	42.3933N/ 117.3950E	21.7/ 285.0	2018–2020	
Chengde-5	42.3937N/ 117.3915E	0.8/ 28.5	2018–2020	
Chengde-6	42.3957N/ 117.3898E	27.0/ 169.8	2018–2020	
Chengde-7	42.3865N/ 117.4005E	32.3/ 155.0	2018–2020	

Geological Survey (USGS) (Woodcock et al., 2008; Wulder et al., 2019). We obtained the Tier 1 (T1, with the highest radiometric calibration and geolocation accuracy) data of Landsat 8 Operational Land Imager (OLI) from USGS (https://earthexplorer.usgs.gov/, last accessed 10/Jul/2022) (Lu et al., 2022; Storey et al., 2014) and derived the Top-of-Atmosphere (TOA) reflectance from the digital numbers using the conversion coefficients included in the Landsat metadata. We used all seven spectral bands of OLI for surface albedo estimation in this study.

2.3. DEM data

DEM describes land surface topographic features, and the free access to fine-resolution DEM data has stimulated many studies in mountains (Bian et al., 2020; Yan et al., 2020). In this study, we selected two widely used DEMs (AW3D30 and SRTM DEM) for DSR and NSR estimation, comparison, and analysis. They both have 1 arc-second resolution (about 30 m in the equator).

AW3D30 DEM was produced by the Panchromatic Remote-sensing Instrument for Stereo Mapping on board the ALOS from January 2006 to April 2011 and released by the Japan Aerospace Exploration Agency (JAXA) in 2015 (Tadono et al., 2014). We downloaded the AW3D30 V3.1 (released in April 2020 and improved in January 2021) from https://www.eorc.jaxa.jp/ALOS/en/aw3d30/index.htm (last accessed 10/Jul/2022).

SRTM DEM was derived using space-borne radar measurements in February 2000, and we used the iterative improvement and void data filling version, the SRTM DEM V003 (JPL 2013), from https://search.earthdata.nasa.gov/ (last accessed 10/Jul/2022).

The nearest neighboring procedure was used to match DEMs and Landsat 8 images (Tan et al., 2015). The slope, aspect, sky view factor (SVF), solar incidence angle, and shadow areas were calculated based on two DEMs. The comparison of topographic information derived from AW3D30 and SRTM DEM for stations in Section 2.1 is shown in Table 2.

2.4. MODIS product

We used MODIS products as inputs for the horizontal direct and diffuse radiation retrieval algorithm. We selected MCD19A2 product (Lyapustin and Wang, 2018) from MODIS Terra and Aqua combined Multi-angle Implementation of Atmospheric Correction for its high resolution and accuracy (Martins et al., 2017; Martins et al., 2019; Superczynski et al., 2017). We used AOD at 0.55 μm and water vapor in MCD19A2 with 1 km resolution. Based on the assumption that atmospheric conditions are reasonably stable in 1 km, the AOD and water vapor products were merged, clipped, and resampled to match Landsat footprints for shortwave radiation estimation.

Table 2
The topographic information derived from AW3D30 and SRTM DEM for stations.

Site name	AW3D30 DEM			SRTM DEM		
	Elevation/ m	Slope/ Aspect(°)	SVF	Elevation/ m	Slope/ Aspect(°)	SVF
Chengde-1	1870	21.6/ 85.3	0.97	1847	17.2/ 58.4	0.98
Chengde-2	1867	17.0/ 291.7	0.98	1839	22.8/ 249.7	0.97
Chengde-3	1890	21.4/ 145.9	0.94	1865	20.1/ 212.7	0.96
Chengde-4	1832	26.9/ 235.0	0.98	1822	19.6/ 259.5	0.98
Chengde-5	1710	1.6/ 126.4	0.96	1714	2.8/ 180.0	0.97
Chengde-6	1792	35.1/ 165.5	0.88	1770	21.3/ 183.3	0.95
Chengde-7	1844	28.3/ 158.5	0.92	1858	33.8/ 150.6	0.92

2.5. Study areas

We selected two Landsat footprints in mountainous areas with different territories for in-depth analysis.

Region 1 is in the eastern Inner Mongolia Autonomous Region border with northeastern Hebei Province in China, where low hills and relatively flat areas dominate the territory. The Worldwide Reference System 2 (WRS2) of region 1 is 122/031 (Path/Row). Region 2 is in the southern Liangshan Yi Autonomous Prefecture of China with Landsat footprint 130/041 (Path/Row). The terrain is complex and mainly covered with mountains and valleys. The low cloud-cover Landsat images were chosen, and the information on the selected study areas and images is shown in Table 3.

3. Methods

3.1. Shortwave radiation estimation in mountains

Fig. 1 shows the flowchart of our DSR and NSR estimation method. The retrieval scheme can be separated into three steps: (i) Estimate surface albedo on sloping terrain by direct estimation method (Ma et al., 2022) based on Discrete Anisotropy Radiative Transfer (DART) model (Gastellu-Etchegorry et al., 2004; Wang et al., 2020) and random forest (RF) regression; (ii) Estimate direct and diffuse radiation on horizontal surfaces based on Second Simulation of a Satellite Signal in the Solar Spectrum vector code (6S) simulations (Vermote et al., 1997) and RF regression, and calculate instantaneous (Landsat 8 overpass time) DSR and NSR using mountain radiative transfer scheme; (iii) Estimate daily mean DSR and NSR by averaging the instantaneous estimation results with 30 min intervals. We validated the RF models' performance using the simulation dataset and verified estimation results against in-situ measured shortwave flux data.

3.1.1. Surface albedo estimation

The traditional topographic correction method was reported to be questionable because of empirical parameters in it (Ma et al., 2021), which may introduce uncertainty into surface parameters retrieval in mountains. We used the direct estimation method for surface albedo (inclined/inclined sloped surface albedo) retrieval (Ma et al., 2022), which directly linked Landsat TOA reflectance data, topographic information, and surface albedo based on DART (Wang et al., 2020) simulation dataset. Here we added the simulations with 0° slope to expand the method for relatively flat areas in mountains. The RF regression has been widely used in remote sensing (Belgiu and Drăguţ, 2016) and was used to describe the nonlinear relationship between inputs and surface albedo.

3.1.2. Instantaneous DSR and NSR estimation on sloping terrains

To estimate DSR and NSR on sloping terrain, the direct and diffuse radiation on horizontal surfaces were estimated firstly by combining radiative transfer simulations and RF regression. We used RF to adopt regression based on the simulation dataset.

Considering the key factors influencing surface DSR (Zhang et al., 2014), we selected solar zenith angle (SZA), aerosol optical depth (AOD), water vapor, elevation, and surface albedo as the variated parameters in 6S simulations. We selected the "US62" atmospheric profile and "Continental" aerosol profile according to previous studies (He et al., 2018a; He et al., 2014). The settings of simulation parameters are shown in Table 4. We trained the RF with 6S simulations using 75% of the simulation dataset and validated the regression using the remaining 25%. We finally derived direct and diffuse shortwave surface radiation by inputting SZA, MODIS AOD, water vapor product (MCD19A2, with merge, clip, and resample processes to 30 m resolution), DEM, and surface albedo estimated in Section 3.1.1.

Table 3
Data acquisition information and terrain parameters for selected study areas and Landsat images. Note that the topographic information is from AW3D30 DEM.

Region	WRS2 PathRow	Center Coordinate	Elevation Range (m)	Median Slope (°)	Time	SZA (°)
1	122031	42°N 118°E	612 – 1741	9.4	20170601	25.4
					20170921	44.1
					20171108	60.1
2	130041	27°N 102°E	1245 – 4354	24.3	20130614	20.5
					20140124	52.7

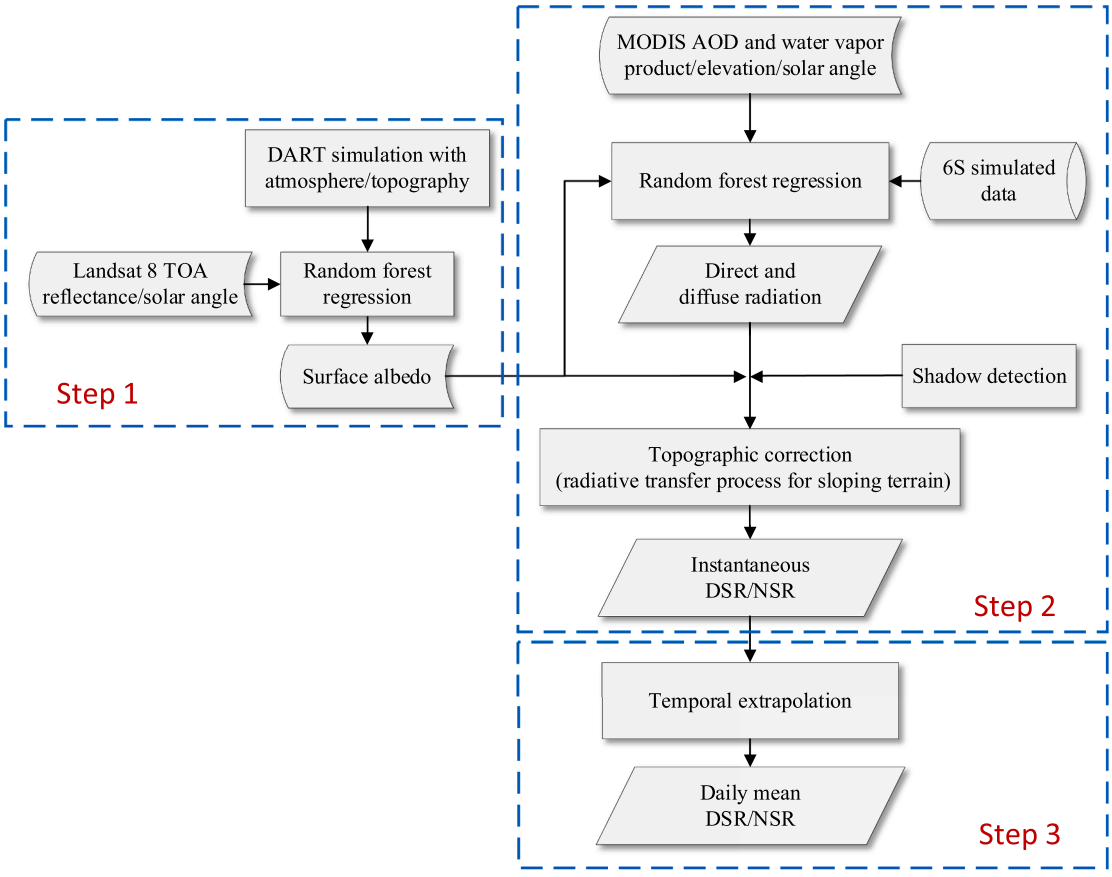

Fig. 1. Flowchart of shortwave radiation estimation method. Three steps include (i) surface albedo estimation; (ii) instantaneous DSR and NSR estimation; (iii) daily mean DSR and NSR generation.

Table 4
The input parameters and range for 6S simulations.

Parameters	Unit	Range
SZA	°	0:1:89
AOD	n/a	0.01, 0.025, 0.05, 0.1, 0.2, 0.4, 0.6
Water vapor	cm	0:0.2:8
Elevation	km	0, 1, 2, 3, 4, 5, 6, 7
Surface albedo	n/a	0, 0.2, 0.4, 0.6, 0.8

Once we obtained the horizontal direct and diffuse radiation, we used the mountain radiative transfer scheme to calculate the DSR on sloping terrain. The total DSR for a single pixel on sloping terrain included three parts Chu et al., 2021; Sandmeier and Itten, 1997): direct radiation, diffuse radiation, and reflected radiation from the surrounding environment, and are expressed as Eqs. (1) to ((4):

$$S^{inst}_{\downarrow,slope} = r_{b,slope} + r_{d,slope} + r_{r,slope}, \quad (1)$$

$$r_{b,slope} = \Theta * r_b * (\cos i / \cos\theta_s), \quad (2)$$

$$r_{d,slope} = r_d * V_d, \quad (3)$$

$$r_{r,slope} = \frac{C_t\overline{\alpha}\cdot\left(r_{b,slope} + r_{d,slope}\right)}{1 - \overline{C_t\alpha}}, \quad (4)$$

where $S^{inst}_{\downarrow,slope}$ refers to the instantaneous DSR on sloping terrain; $r_{b,slope}$, $r_{d,slope}$ and $r_{r,slope}$ are direct radiation, diffuse radiation, and reflected radiation from surrounding pixels on sloping terrain, respectively; r_b and r_d refer to the horizontal direct and diffuse radiation, respectively; Θ is the shadow factor, which equals 1 when the pixel was not shadowed and equals 0 when shadowed, and the shadow detection algorithm based on the relationship between solar ray and surrounding topography (Li et al., 2002; Zhang et al., 2018); i refers to the solar incidence angle for sloping terrain; θ_s refers to the solar zenith angle; V_d refers to the SVF; α refers to the surface albedo. C_t is the terrain configuration factor and can be calculated as $C_t = 1 - V_d$. The average of values in Eq. (4) is calculated by a 2700 m × 2700 m sliding window (Chu et al., 2021).

The cosine of solar incidence angle is defined as Eq. (5) (Horn, 1981):

$$\cos i = \cos\theta_s\cos S + \sin\theta_s\sin S\cos(\varphi_a - \varphi_0), \quad (5)$$

where S is the slope angle, φ_a is the solar azimuth angle, and φ_0 is the aspect angle of the terrain. The slope and aspect of the terrain were calculated with a 3 × 3 pixel window (Horn, 1981).

We used the typical method (Dozier and Frew, 1990) to calculate SVF, which is based on Eq. (6):

$$V_d = \frac{1}{N}\sum_{i=1}^{N}\left[\cos S\sin^2 H_{\varphi_i} + \sin S\cos(\varphi_i - \varphi_0)(H_{\varphi_i} - \sin H_{\varphi_i}\cos H_{\varphi_i})\right], \quad (6)$$

where N is the number of discretized search directions, φ_i is the azimuth angle of direction i, and H_{φ_i} is defined from the zenith downward to the local horizon over the unobstructed hemisphere in direction φ_i.

We obtained instantaneous DSR on sloping terrain based on the above parameterization scheme. Then, the instantaneous NSR could be simply achieved through Eq. (7):

$$S^{inst}_{n,slope} = S^{inst}_{\downarrow,slope} * (1-\alpha). \quad (7)$$

3.1.3. Daily mean DSR and NSR calculations

Compared with instantaneous DSR and NSR, the daily mean radiation is more important for studying surface energy budget and mountain climate change (Bisht et al., 2005; Yan et al., 2018). The daily mean DSR and NSR could be computed as averaging the integral of instantaneous DSR and NSR from Section 3.1.2 over the daytime with the assumption that the atmospheric conditions are fairly invariant during the day (Wang et al., 2015):

$$S^{daily}_{\downarrow,slope} = \frac{\int S^{inst}_{\downarrow,slope}(t)dt}{T}, \quad (8)$$

$$S^{daily}_{n,slope} = \frac{\int S^{inst}_{n,slope}(t)dt}{T}, \quad (9)$$

where T is the length of a day (24 h), $S^{inst}_{\downarrow,slope}(t)$ and $S^{inst}_{n,slope}(t)$ are estimated by variation of SZA in a day, and the interval of t was set to 30 min. With this method, we could capture the diurnal variation of shortwave radiation in a day with topographic consideration (e.g., variation of shadow areas and solar incident angle).

3.2. DEM uncertainty analysis

Fig. 2 shows the flowchart for evaluating the impacts of DEM uncertainty on shortwave radiation in mountains. We first validated the estimated shortwave radiation based on in-situ measured topographic information, SRTM DEM, and AW3D30 DEM against *in-situ* measured shortwave flux (Section 4.2). Then, we compared the shortwave radiation mapping results using SRTM and AW3D3D DEMs (Section 4.3). Finally, based on the assessment of DEMs (Carrera-Hernández, 2021; Liu et al., 2019), we introduced random errors into AW3D30 (as the "reference" value here) to find how large shortwave radiation errors could be caused by DEM uncertainty (Section 4.4). Note that the evaluation and comparison in Sections 4.3 and 4.4 were based on different spatial resolutions.

The scaling-up of fluxes in mountains was suggested to consider the surface areas weight Wang et al., 2018; Yan et al., 2016) based on Eqs. (10) and ((11):

$$S^{coarse} = \sum_{i=1}^{N} p_i \cdot S_i^{fine}, \quad (10)$$

$$p_i = A_i \Big/ \sum_{i=1}^{N} A_i, \quad (11)$$

where S^{coarse} and S_i^{fine} are the coarse and fine-scale shortwave radiation, respectively, A_i is the surface area for DEM pixel i based on Jenness (2004), and p_i is the area-weighted ratio derived from dividing the surface area for the fine-resolution pixel i to the total surface area of the coarse pixel.

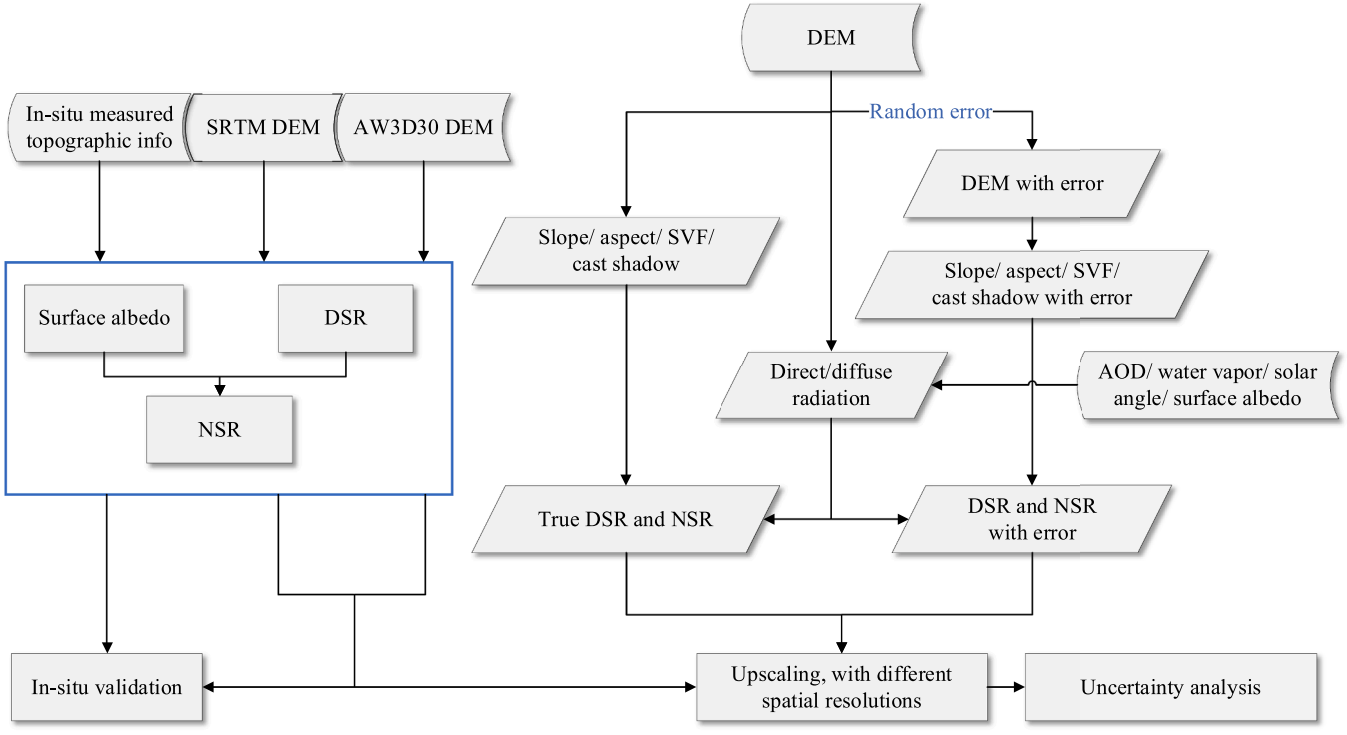

Fig. 2. Flowchart of evaluating the impacts of DEM uncertainty on shortwave radiation in mountains.

4. Results

4.1. Performance of random forest regressions

We validated the RF regression's performance in predicting direct radiation, diffuse radiation, and surface albedo using the simulation dataset, shown in Table 5. RF provided satisfactory regression performance in both training and validation datasets, where R^2 were higher than 0.98 for all these validations, and RMSEs were lower than 1.3W / m^2 and 0.6W/m^2 for direct and diffuse radiation, respectively, while that was lower than 0.004 for surface albedo.

4.2. Comparison of validation results against in-situ measurements

Fig. 3 shows the validation against in-situ measurements in terms of instantaneous (Landsat 8 overpass time) DSR and NSR, daily mean DSR and NSR and surface albedo using in-situ measured topographic parameters. The comparison of the estimated and measured shortwave radiation illustrated the potential of our estimation method: $R^2 = 0.92$, RMSE = 65.9 W/m^2 and bias = 21.1 W/m^2 for instantaneous DSR; $R^2 = 0.95$, RMSE = 21.2W/m^2 and bias = 10.2W/m^2 for daily mean DSR; $R^2 = 0.90$, RMSE = 65.1W/m^2 and bias = 16.5W/m^2 for instantaneous NSR; $R^2 = 0.94$, RMSE = 22.5W/m^2 and bias = 11.1W /m^2 for daily mean NSR; $R^2 = 0.53$, RMSE = 0.027 and bias = 0.004 for surface albedo.

We also used the topographic information derived from SRTM and AW3D30 DEMs to estimate shortwave radiation, and their validation against in-situ measured shortwave flux and surface albedo are shown in Table 6 where the validation of the algorithm without topographic consideration (assuming flat areas) is also offered. Compared to Fig. 3, sharp deterioration appeared in the validation of shortwave radiation using topographic data derived from both DEMs, especially for instantaneous DSR and NSR where RMSEs increased from 65.9W /m^2 to 96.9W/m^2 and 108.1W/m^2 for DSR (errors increased 47.0% and 64.0%), and 65.1W/m^2 to 91.0W/m^2 and 98.5W/m^2 for NSR (39.8% and 51.3%) when using SRTM and AW3D30 DEMs, respectively. The RMSEs of daily mean DSR could increase from 21.2W /m^2 to 30.1W /m^2 and 31.0W/m^2 (42.0% and 46.2%), and it increased from 22.5W /m^2 to 29.3W/m^2 and 30.5W/m^2 for daily mean NSR (30.2% and 35.6%) when using SRTM and AW3D30 DEMs, respectively. However, there was no noteworthy change for albedo, where RMSEs equaled 0.027 and 0.029 based on two DEMs. Meanwhile, we evaluated the algorithm neglecting topography (considered as flat areas), representing the worst condition of DEM uncertainty; the validation results were poor where RMSEs of instantaneous DSR, daily mean DSR, instantaneous NSR, daily mean NSR, and surface albedo equaled 198.7W/m^2, 55.5W /m^2, 189.3W /m^2, 52.6W/m^2, and 0.037, respectively.

To better understand the shortwave radiation in mountains and check out the possible issues to impact the estimation results, we gave an example of the in-situ measured and estimated shortwave radiation in a day (Fig. 4). In Fig. 4, the diurnal variation of shortwave radiation all showed considerable differences from that neglecting topography, and the peak value and the time of the peak substantially differed in these stations. With local topographic measurements, the estimated shortwave radiation could capture the daily variation and provide reliable accuracy. However, the estimations from AW3D30 and SRTM DEMs showed some deviations compared with in-situ measured data, such as stations 2 and 3. The shadow in mountains would cause a dramatic reduction in shortwave radiation under clear sky, and our method could also capture the shortwave radiation in the shadowed ground (in stations 5 and 6). We have tried to avoid data with cloud contaminations, but considering the limited number of in-situ measured shortwave flux data, some data with slight cloud contaminations were still included (at stations 1, 6, and 7).

Table. 5
Training and validation accuracy for RF regressions (the units of RMSE and bias for direct and diffuse radiation are W/m^2).

Parameters	Training accuracy			Validation accuracy		
	R^2	RMSE	bias	R^2	RMSE	bias
Direct radiation	1.00	0.5	0.0	1.00	1.3	0.1
Diffuse radiation	1.00	0.3	0.0	1.00	0.6	0.0
Surface albedo	1.00	0.002	0.000	0.98	0.004	0.000

4.3. Shortwave radiation deviations caused by diverse DEMs

In Section 4.2, there were noteworthy shortwave radiation deviations based on different sources of topographic information. Therefore, we adopted a comparison of SRTM and AW3D30 DEMs for shortwave radiation estimation in the selected Landsat 8 images (Section 2.5). The differences between SRTM and AW3D30 DEMs and the derived slope and aspect in the selected two footprints are shown in Fig. 5. The differences between DEM, slope, and aspect were almost unbiased. The DEM root-mean-square deviations (RMSDs) were 7.1 m and 14.9 m in two Landsat footprints, and the deviation of aspect (RMSD = 45.6° and 28.4°) was larger than that of slope (RMSD = 4.5° and 6.2°). We estimated DSR and NSR using topographic information derived from these two DEMs, respectively, and the comparison is shown in Fig. 6. We did not declare which result was better but focused on their difference. The difference between DSR and NSR was scene-dependent, where relative RMSD (rRMSD) could vary from 3.4% to 16.8% (RMSD from 36.6W/m^2 to 103.6W/m^2) for instantaneous DSR, 2.3% to 13.0% (9.1W/m^2 to 25.8W/m^2) for daily mean DSR, 3.5% to 16.3% (31.7W/m^2 to 83.8W/m^2) for instantaneous NSR, and 2.6% to 12.5% (8.9W/m^2 to 20.6W/m^2) for daily mean NSR. In general, the difference arose from summer to winter, and a more considerable difference occurred in Landsat footprint "130/041" (with steeper terrain) than "122/031". To better observe the difference using AW3D30 and SRTM DEM, we show the scatter plot of instantaneous and daily mean NSR using two DEMs in Fig. 7. In Fig. 7, the bias was small (7.9W/m^2 and 2.7W/m^2); however, the points were very discrete; thus, RMSD was high (83.8W/m^2 and 20.6W/m^2).

We upscaled the fine-spatial-resolution (30 m) to coarse-spatial-resolution shortwave radiation to figure out the relationship between the spatial resolution of resulting retrievals and deviations. We upscaled shortwave radiation from 30 m to 120 m, 240 m, 480 m, 960 m, and 3000 m and compared the deviations derived from two DEMs, shown in Fig. 8 (we only show NSR here because of similar results of NSR and DSR). The deviations of shortwave radiation decreased considerably with a coarser scale: when up-scaled to 120 m, the maximum deviations decreased from 16.3% (83.8W/m^2) to 7.1% (36.6W/m^2) for instantaneous NSR, and 12.5% (20.6W/m^2) to 5.9% (9.8W/m^2) for daily mean NSR; the deviations of instantaneous and daily mean NSR could be lower than 1.8% (9.3W/m^2) and 1.8% (5.6W/m^2) with the spatial resolution at 3000 m.

4.4. Quantifying shortwave radiation uncertainty from DEM errors

We further quantitatively evaluated retrieval uncertainty caused by DEM errors. We took AW3D30 DEM as the "reference" data, introduced the Gaussian random errors into it, and compared estimation results using these DEM with errors and "reference" DEM. Based on Carrera-Hernández (2021), the MAE of random error was set as 1.0 m, 2.5 m, 5 m, and 7.5 m. The comparison of NSR results using reference DEM and DEM with random errors in different resolutions is shown in Fig. 9. In Fig. 9, the NSR difference depended on the image and achieved a higher difference in wintertime. The deviations increased with random errors and decreased with spatial resolution. NSR difference on instantaneous and daily mean values at 30 m spatial resolution could reach 33.6%

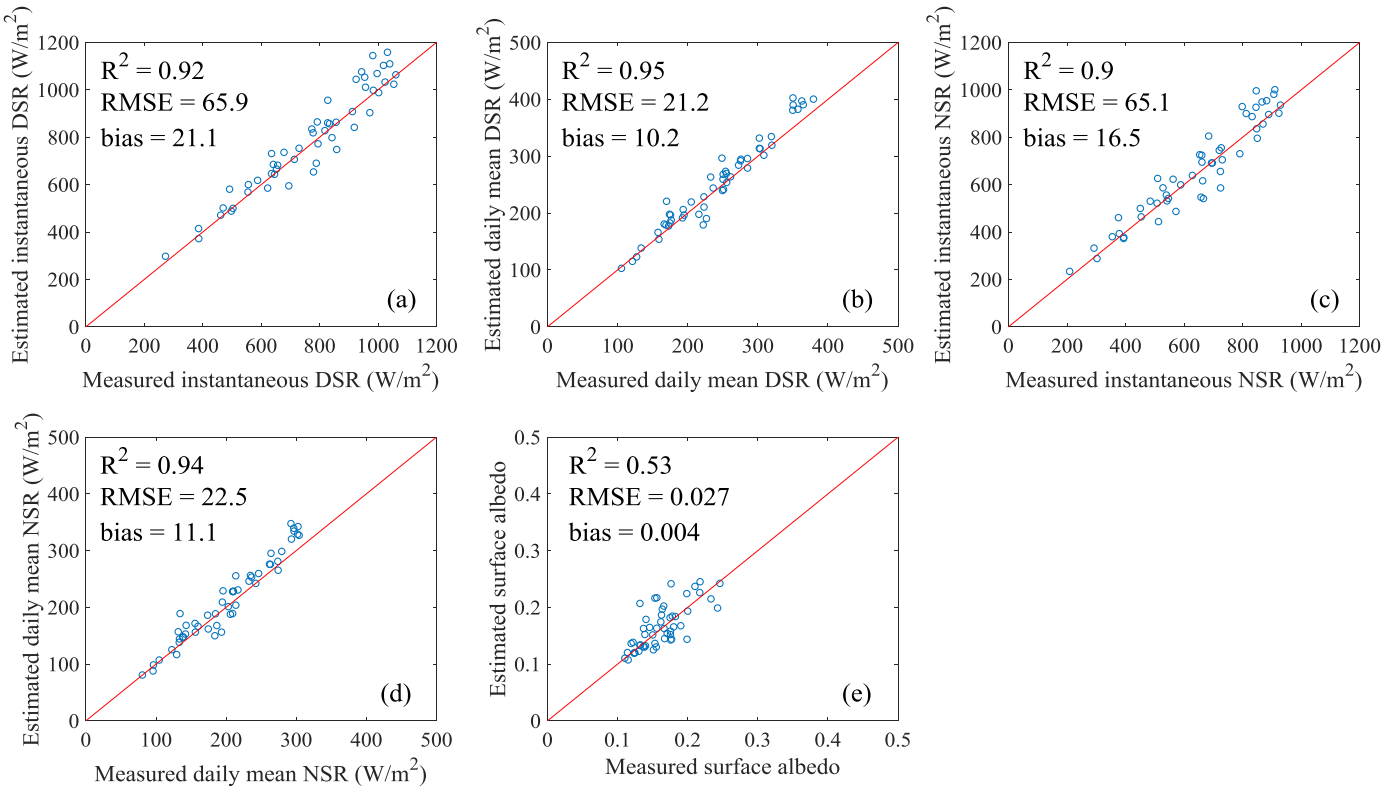

Fig. 3. Validation of estimated DSR, NSR, and surface albedo against in-situ measurements using the measured slope and aspect. (a) Instantaneous DSR, (b) daily mean DSR, (c) instantaneous NSR, (d) daily mean NSR, and (e) surface albedo.

Table 6
Validation results using SRTM and AW3D30 DEM and without DEM, respectively.

DEM used	Parameters	R^2	RMSE (W/m^2)	Bias (W/m^2)
SRTM DEM	Instantaneous DSR	0.79	96.9	19.3
	Daily mean DSR	0.87	30.1	9.4
	Instantaneous NSR	0.79	91.0	14.1
	Daily mean NSR	0.85	29.3	10.1
	Albedo	0.51	0.027	0.005
AW3D30 DEM	Instantaneous DSR	0.84	108.1	61.1
	Daily mean DSR	0.87	31.0	11.2
	Instantaneous NSR	0.84	98.5	54.5
	Daily mean NSR	0.86	30.5	13.6
	Albedo	0.43	0.029	−0.003
Without DEM (flat)	Instantaneous DSR	0.23	198.7	−49.7
	Daily mean DSR	0.60	55.5	−17.0
	Instantaneous NSR	0.22	189.3	−45.4
	Daily mean NSR	0.54	52.6	−12.1
	Albedo	0.12	0.037	0.005

($143.8W/m^2$) and 28.8% ($31.5W/m^2$) with MAE of random errors equaled 7.5 m; they could reach 19.8% ($89.1W/m^2$) and 17.0% ($19.6W/m^2$) when MAE = 5.0 m; they were lower than 8.0% ($36.9W/m^2$) and 7.2% ($8.6W/m^2$) for MAE = 2.5 m; for MAE = 1.0 m, NSR differences were lower than 3.3% ($15.5W/m^2$) and 2.6% ($3.2W/m^2$) in the selected images. The deviations decreased by more than 50% when images were upscaled from 30 m to 120 m. The deviations on instantaneous and daily mean NSR could reach 8.9% ($38.0W/m^2$) and 10.2% ($11.2W/m^2$) when MAE = 7.5 m at 3000 m spatial resolution; and they decreased to 0.3% ($1.4W/m^2$) and 0.5% ($1.6W/m^2$) when MAE = 1.0 m.

5. Discussion

5.1. Shortwave radiation estimation in mountains

In our study, we employed a clear-sky instantaneous and daily mean shortwave radiation (DSR and NSR) estimation method as the proxy to evaluate the impacts of DEM uncertainty on shortwave radiation in mountains. The validation against in-situ measurements verified our method's feasibility (Fig. 3). Furthermore, our method depended on AOD and water vapor inputs, and some bias appeared, which may be caused by their uncertainty (Martins et al., 2017; Superczynski et al., 2017). Owing to our assumption that the atmospheric condition is fairly stable, bias may be introduced (Fig. 3) under slight cloud contaminations (Fig. 4). However, these problems did not have a great impact on the evaluation results of DEM uncertainty on shortwave radiation in mountains.

Our study showed great deviations when ignoring topographic effects (Table 6), consistent with previous studies (Aguilar et al., 2010; Helbig and Löwe, 2012; Lee et al., 2013; Shi and Xiao, 2021). We also showed instantaneous and daily mean NSR mapping using our method (Fig. 10), and there was remarkable heterogeneity for both instantaneous and daily mean results which grew from summer to winter. Fig. 4 typically showed how topographic effects influenced shortwave radiation: (i) The peak of diurnal shortwave radiation did not appear at local noon but depended on the terrain, and the peak values greatly differed from that in flat areas; (ii) The shadow would cause dramatic reductions for shortwave radiation in clear sky; thus, the capture of shadow areas was essential. The phenomena above also illustrated different sunrise and sunset time for different locations in mountains (Zhang et al., 2018), indicating why the temporal extrapolation method for flat areas was not suitable for mountainous areas (Yan et al., 2018).

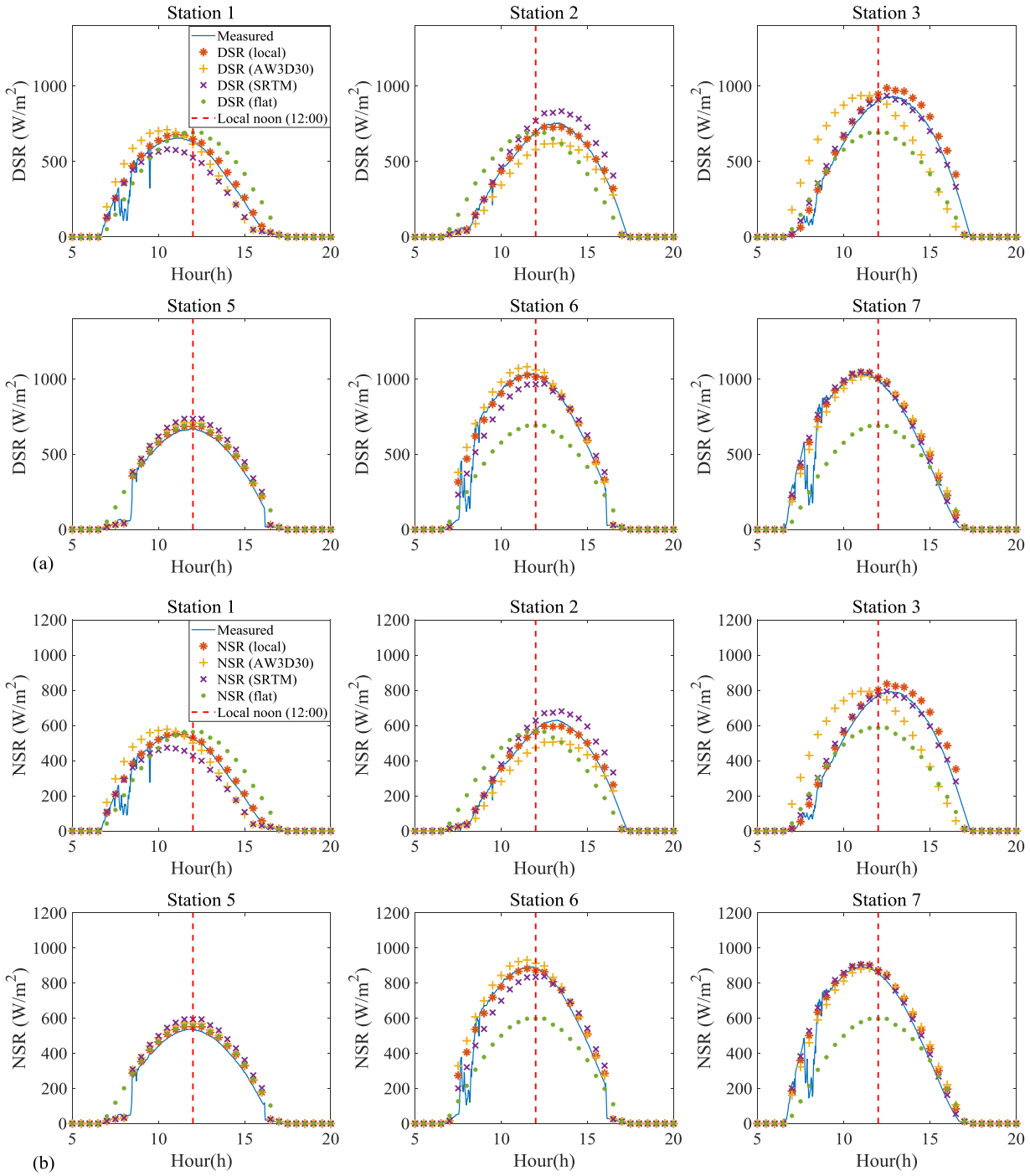

Fig. 4. In-situ measured and estimated shortwave radiation variation on October 22, 2020. (a) DSR, (b) NSR. The red dotted line refers to the local noon.

5.2. *Impacts of DEM uncertainty on shortwave radiation in mountains*

Some studies have highlighted the impacts of DEM resolution (Huang et al., 2017) and geolocation bias (Hao et al., 2019b; Wu et al., 2022) on shortwave radiation parameters, and our study quantitatively evaluated how large uncertainty could be introduced into shortwave radiation at diverse spatial and temporal resolutions from DEM deviations. Our study showed that the RMSEs were larger when using SRTM and AW3D30 DEMs than in-situ measured topographic information (Fig. 3 and Table 6), especially for instantaneous results (the RMSE could increase by 64.0%). The main reason was that the bias in slope and aspect would lead to the shift of shortwave radiation in a day (Fig. 4). For example, there was an offset of estimated diurnal DSR and NSR in stations 2 and 3 of Fig. 4 using AW3D30 and SRTM DEM compared with in-situ measured data, thus resulting in considerable deviations for instantaneous estimations. The deviations could be mitigated when aggregated to daily mean values because the topographic effects could be lessened with diurnal variations of the sun (Fig. 10); while the errors for daily mean DSR estimation could also increase by 46.2% (Table 6). The algorithm neglecting topographic effects (Table 6) can represent the largest impacts of DEM uncertainty on shortwave radiation estimation in mountains. The results of albedo estimation demonstrated the need for the consideration of topography in the retrieval process as shown in Table 6, which has been documented in our earlier study (Ma et al., 2022). In comparison, the choice of DEM (SRTM or AW3D30) led to a slight difference of 0.002 in the RMSE of albedo estimation. Our study

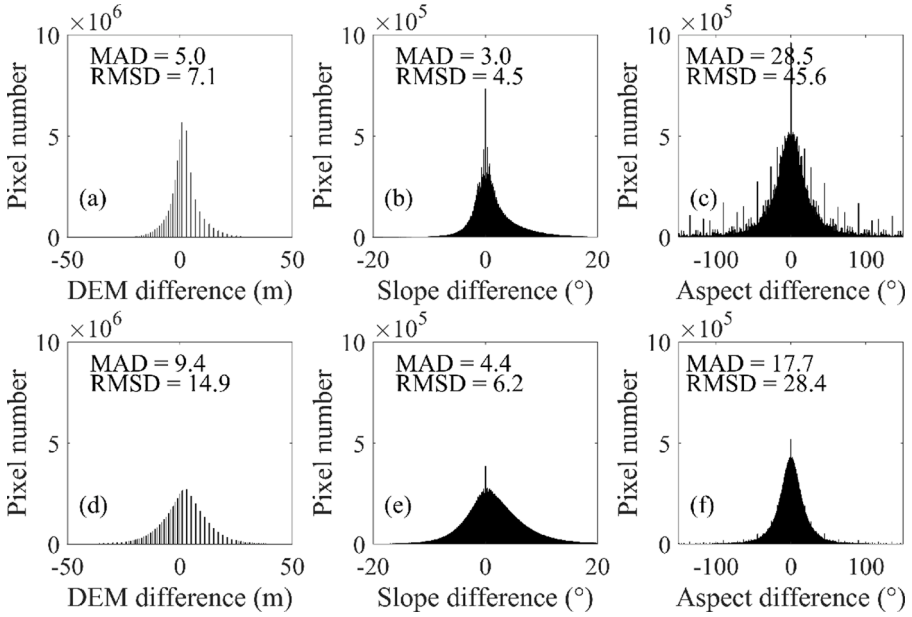

Fig. 5. Differences of SRTM and AW3D30 DEMs and the derived slope and aspect for two Landsat footprints. (a), (b) and (c) are the DEM, slope, and aspect difference in Landsat footprint 122/031 (Path/Row), respectively; (d), (e), and (f) are the DEM, slope, and aspect difference in Landsat footprint 130/041. The difference is calculated as AW3D30 DEM, slope, and aspect minus SRTM DEM, slope, and aspect, respectively. MAD = mean absolute deviation.

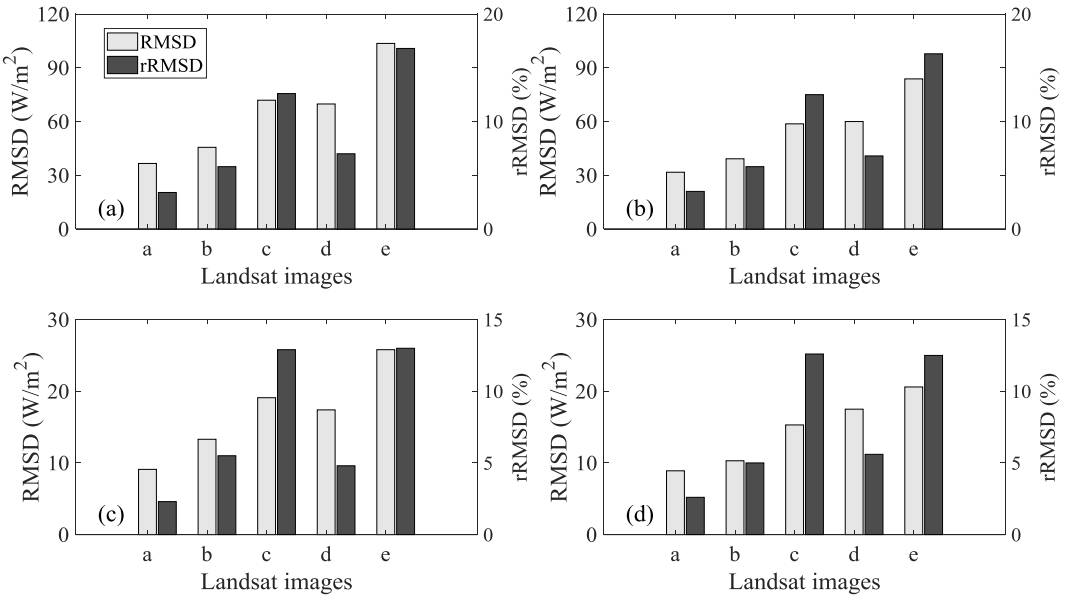

Fig. 6. The comparison of DSR and NSR results using different DEMs. (a) Instantaneous DSR, (b) instantaneous NSR, (c) daily mean DSR, and (d) daily mean NSR. The a to e in x axis refer to different Landsat images (PathRow_time): 122031_20170601, 122031_20170921, 122031_20171108, 130041_20130614, 130041_20140124.

also corresponded with Mira et al. (2016) that the uncertainty of NSR mainly comes from DSR estimation.

The shortwave radiation differences based on SRTM and AW3D30 DEMs could reach 13.0% (71.9W/m^2) and 13.2% (19.6W /m^2) for instantaneous and daily mean DSR in winter (Fig. 6) with smooth terrain (average slope equals 9.4° for Landsat 8 path/row 122/031), while these values could reach 16.8% (103.6W/m^2) and 13.0% (25.8W /m^2) for steeper terrains (Landsat 8 path/row 130/041). Generally, shortwave radiation differences using AW3D30 and SRTM DEMs increased from summer to winter, which could be explained by shortwave radiation being more sensitive to topographic information with larger SZA. With Eqs. (2) and (5), the direct radiation in mountains was linearly correlated with $\cos S + \sin\theta_s \sin S \cos(\varphi_a - \varphi_0)\,/\cos\theta_s$ for non-shadow areas, and when SZA became larger, the influence of topography was larger. Meanwhile, when SZA became larger, the shadow areas became larger, and the misclassifying shadow and non-shadow areas would yield remarkable differences in shortwave radiation. For example, the misclassification of shadow and non-shadow areas led to terribly discrete points in instantaneous results in Fig. 7 (a), while these errors decreased for daily mean values (Fig. 7 (b)).

It is hard for researchers to determine which DEM to use and realize how large errors would be caused by DEM uncertainty because the performance of DEM depends on many factors, such as land cover, elevation, slope, and aspect (Carrera-Hernández, 2021). We compared

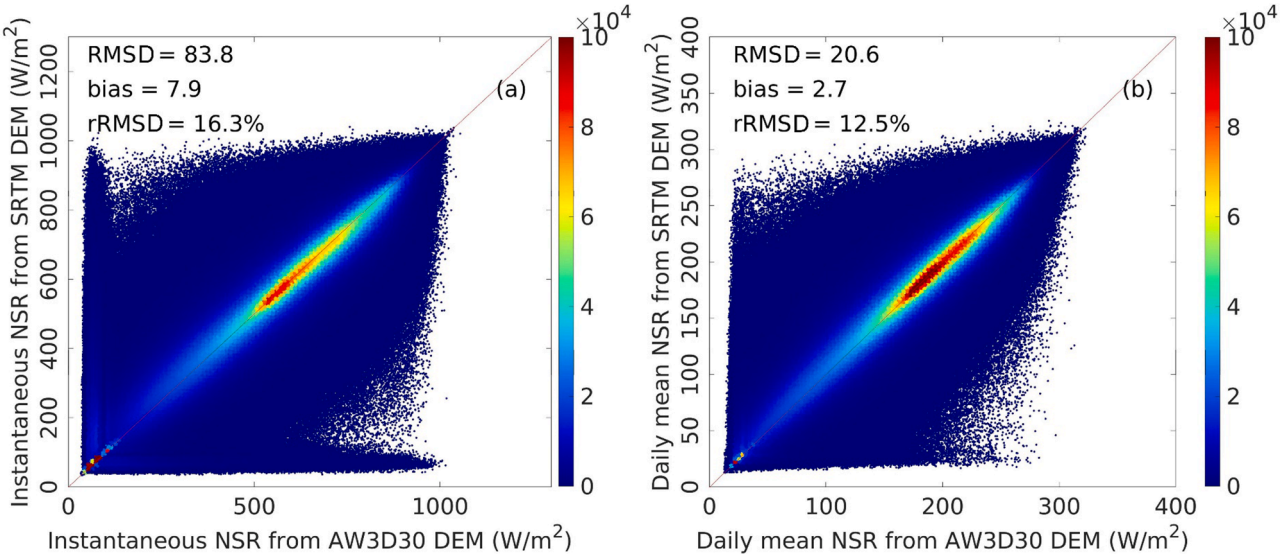

Fig. 7. Comparison of NSR estimations using two DEMs in Landsat 8 footprint 130/041 (path/row) on 24/Jan/2014.

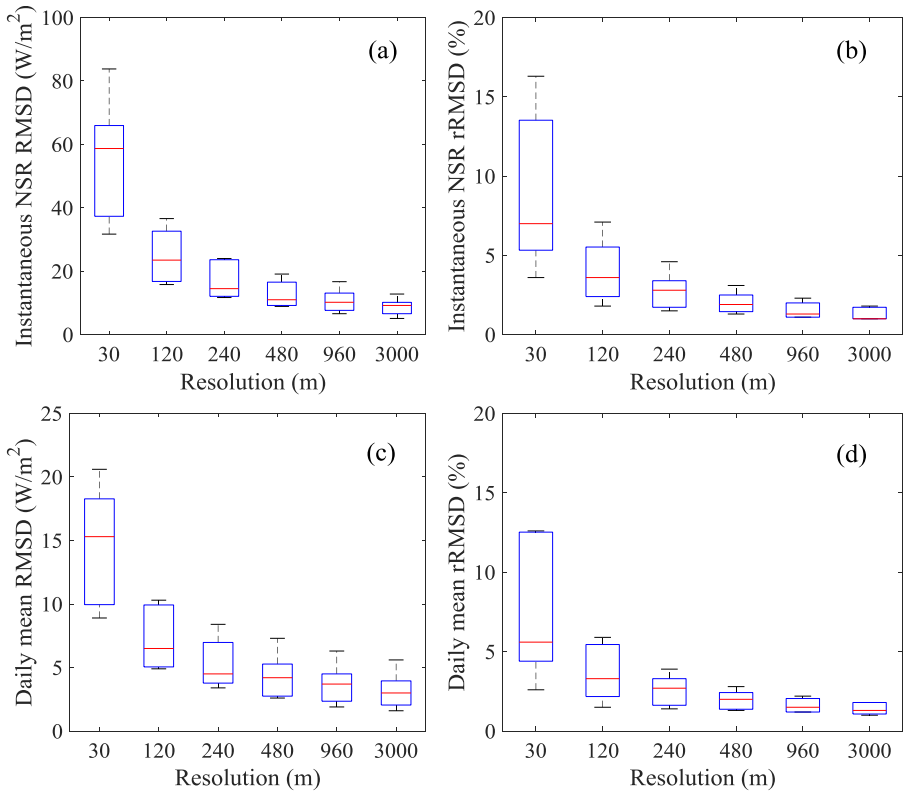

Fig. 8. Boxplot of NSR deviations from SRTM and AW3D30 DEMs with diverse spatial resolutions. (a) instantaneous NSR RMSD based on two DEMs, (b) instantaneous NSR rRMSD, (c) daily mean NSR RMSD, and (d) daily mean NSR rRMSD.

the DEM with random errors to understand the uncertainty of shortwave radiation caused by DEM errors. When MAE of random error equaled 2.5 m, the instantaneous and daily mean NSR difference could reach 8.0% (36.9W/m^2) and 7.2% (8.6W/m^2) in winter, 19.8% (89.1W /m^2) and 17.0% (19.6W/m^2) when MAE = 5.0 m, and 33.6% (143.8W /m^2) and 28.8% (31.5W/m^2) when MAE = 7.5 m. Considering the validation results with in-situ measured topographic information as the algorithm's accuracy (Fig. 3), with DEM MAE equaling about 5.0m, the errors caused by DEM could exceed the algorithm uncertainty itself in winter. Moreover, the MAD between SRTM and AW3D30 DEMs equaled 5.0 m and 9.4 m in the selected two Landsat footprints (Fig. 5). Therefore, this indicated that the shortwave radiation deviations caused by diverse DEMs could dominate the overall uncertainty at 30 m spatial scale. Although AW3D30 DEM was reported to have the highest accuracy, whose MAE equaled about 2.5 m (Carrera-Hernández, 2021), studies have declared lower DEM accuracy with slope increasing (Jing et al., 2014; Zhan et al., 2021). For example, Carrera-Hernández (2021) reported that the MAE of AW3D30 could reach 4.1 m, 4.8 m, and 5.9 m for slopes from 30° to 35°, 35° to 40°, and 40° to 45°, respectively. Liu et al. (2019) reported that the MAE of AW3D30 could exceed 4.5 m and 8.0 m

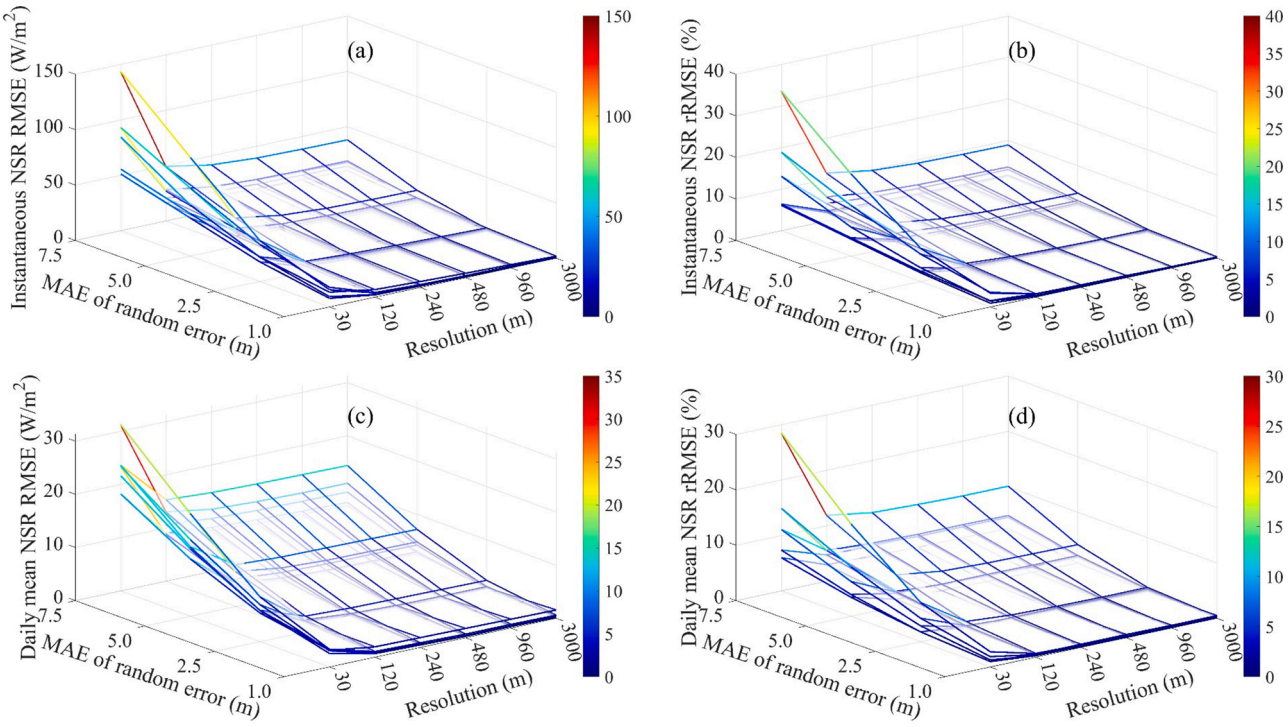

Fig. 9. Difference of estimated NSR using DEM with random errors and reference DEM at different spatial resolutions. The five layers represent the five selected Landsat images. (a) Instantaneous NSR RMSE, (b) instantaneous NSR relative RMSE (rRMSE), (c) daily mean NSR RMSE, and (d) daily mean NSR rRMSE.

for slopes larger than 30° and 40°, respectively. Meanwhile, the accuracy of void areas of DEMs was low (MAE = 11.89 m for void areas of AW3D30) (Liu et al., 2019). For the reasons above, the current free-available DEM may not provide sufficient accuracy for fine-spatial-resolution shortwave radiation applications in steep terrain. Meanwhile, although the DEM was in 30 m resolution, the effective resolution of slope and aspect is 90 m, as they calculated with a 3 × 3 window size (Horn, 1981; Jones, 1998), which makes it hard to capture drastic topographic variations, such as valleys and peaks. Vaze et al. (2010) also suggested using high-resolution DEM instead of conventional low-resolution DEM. Therefore, fine-spatial-resolution and high-accuracy shortwave radiation mapping in mountains largely relied on the resolution and accuracy of DEM.

We found large deviations in shortwave radiation caused by DEM errors in fine-spatial-resolution data (30 m), but deviations could decrease with an increase in spatial scale (Figs. 8 and 9). The shortwave radiation deviations could decrease by more than 50% when upscaled from 30 m to 120 m. With the spatial resolution equaling 3000 m, the relative shortwave radiation deviations were lower than 2%. The reason was that the errors of fine-scale topographic information would neutralize in coarse-spatial-resolution pixels. Therefore, fine-spatial-resolution shortwave radiation mapping could be a crucial bridge for validating coarse-scale products in mountains.

Although our evaluation only included the algorithms we developed in this study, the results were universal because the key ideas to describe topographic effects were almost the same Amatya et al., 2015; Chu et al., 2021; Wang et al., 2018), which were based on the traditional mountain radiative transfer process (Eqs. (1) to ((4)) (Sandmeier and Itten, 1997). Generally, DEM errors would be propagated to topographic information, especially slope and aspect (Fig. 5), because slope and aspect depend on the deviation of surrounding pixels (Horn, 1981), and relatively small errors in DEM would result in large deviations for slope and aspect (Wang and Wang, 2015), and thus incident angle (Eq. (5)). Shadow detection results were also sensitive to DEM (Zhang et al., 2018) and seriously impacted direct radiation (Eq. (2)). The direct radiation dominates in clear sky, thus the uncertainty in incident angle and shadow detection largely influenced shortwave radiation estimation in mountains (Eq. (2)).

5.3. Limitations and future study

The limited slope-parallel in-situ measured data hinders the validation of algorithms and understanding of shortwave radiation in mountains. In addition to errors in topographic information outlined in our paper, the sensor tilt could lead to non-negligible errors in the measured data (Bogren et al., 2016). Thus, high-quality slope-parallel measurements in mountains are hard to obtain but urgently needed.

Our study focused on clear sky conditions because the current cloudy-sky shortwave radiation estimation in mountains is considerably challenging (Chen et al., 2012; Helbig et al., 2010; Letu et al., 2020). Meanwhile, the topographic effect in clear sky was more remarkable than cloudy sky (Zhang et al., 2019), and larger uncertainty was caused by DEM errors for clear-sky shortwave radiation. Therefore, our study could basically point out the worst circumstance of how DEM errors influence shortwave radiation uncertainty in mountains. Due to the high cloud cover in mountains, clear-sky data included in this study was limited. While the major findings would not change, more data over other areas, if available, could generate more accurate error analysis results.

Some studies have reported large errors of shortwave radiation products in rugged terrain (Shi and Liang, 2013; Yang et al., 2008), and point measurements in complex terrain could not depict the coarse-scale flux. We found relatively small uncertainty caused by DEM errors for coarse spatial resolution shortwave radiation estimation; thus, it was feasible to further validate coarse-scale satellite products using fine-scale mapping in mountains.

6. Conclusion

To better understand energy budget in mountainous areas, this paper explored the impacts of DEM uncertainty on shortwave radiation in mountains at diverse spatial and temporal scales. We derived instanta-

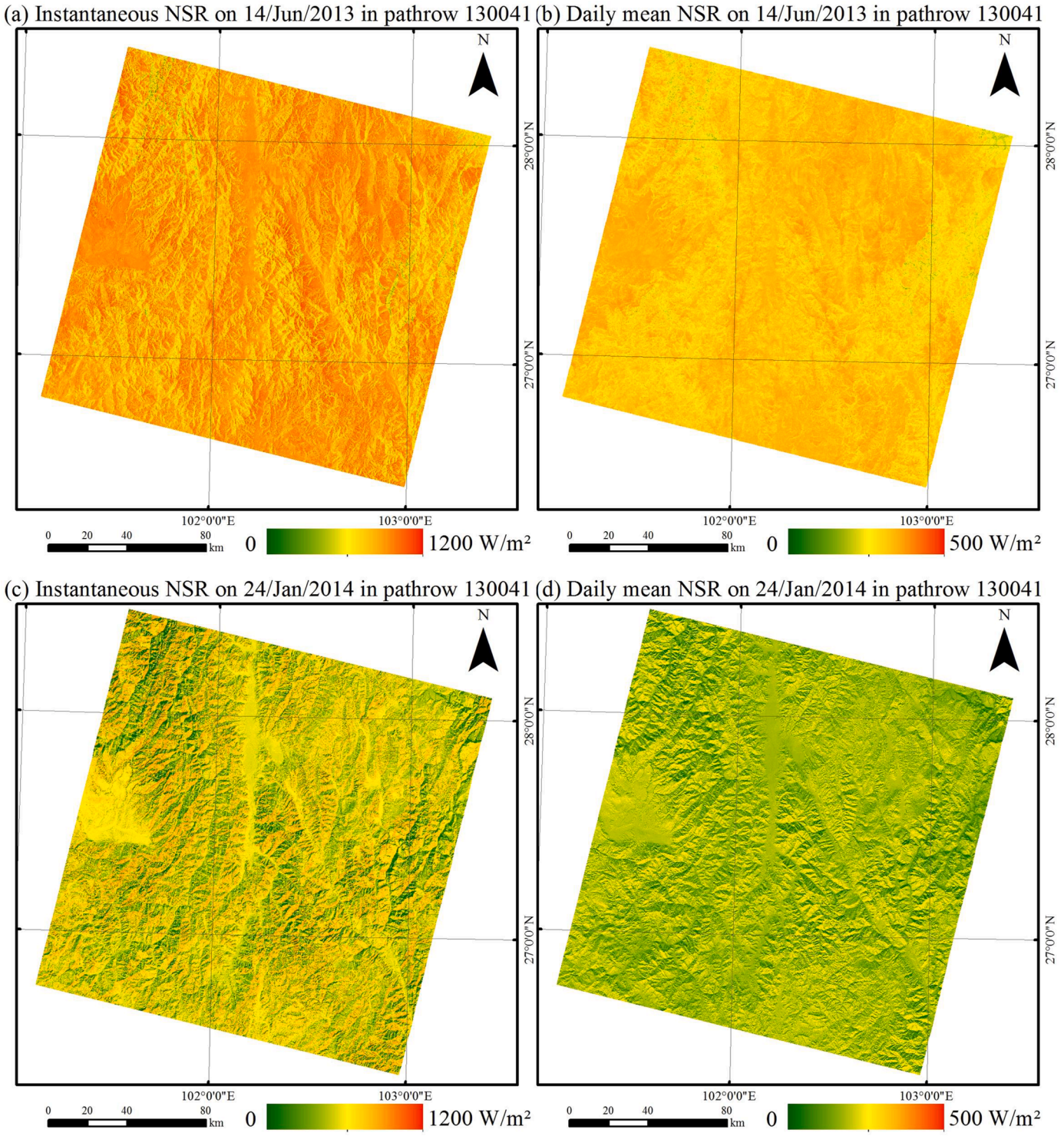

Fig. 10. Instantaneous and daily mean NSR in mountains based on AW3D30. (a) and (b) are instantaneous and daily mean NSR in 130/041 (Landsat 8 path/row) on 14/Jun/2013, respectively; (c) and (d) are instantaneous and daily mean NSR in 130/041 (Landsat 8 path/row) on 24/Jan/2014, respectively.

neous DSR using MODIS atmospheric products with the mountain radiative transfer process, directly estimated surface albedo with topographic consideration, and calculated NSR using the estimated DSR and albedo. The daily mean DSR and NSR were calculated by the integral of the instantaneous estimations in a day. The feasibility of the algorithm was verified against in-situ measured shortwave flux data: RMSEs of 65.9 W/m^2 and 65.1 W/m^2 for instantaneous DSR and NSR, respectively; 21.2 W/m^2 and 22.5 W/m^2 for daily mean DSR and NSR values. We implemented our evaluation based on this method, while our evaluation results were universal to mountainous shortwave radiation modeling and estimation fields.

When using SRTM and AW3D30 DEMs for estimation and validation, the RMSE of instantaneous and daily mean DSR (similar magnitude for NSR) could increase by 64.0% (from 65.9 W/m^2 to 108.1 W/m^2) and 46.2% (from 21.2 W/m^2 to 31.0 W/m^2) compared with results using in-situ measured topographic parameters. The instantaneous and daily mean DSR deviations using SRTM and AW3D30 DEMs could reach

16.8% (103.6 W/m^2) and 13.0% (25.8 W/m^2) in wintertime. The differences increased from summer to winter and decreased with coarser spatial resolution, which could reach 16.3% (83.8 W /m^2) and 12.5% (20.6 W/m^2) in 30 m and 1.8% (9.3 W/m^2) and 1.8% (5.6 W /m^2) in 3000 m for instantaneous and daily mean NSR, respectively. We quantitatively studied this uncertainty by evaluating shortwave radiation using DEM with random errors: instantaneous and daily mean NSR uncertainty could reach 8.0% (36.9 W/m^2) and 7.2% (8.6 W /m^2) when MAE of random error equaled 2.5 m. The shortwave radiation uncertainty caused by DEM may exceed the algorithm uncertainty itself with DEM MAE equaling about 5.0 m. Considering the current DEM accuracy (about 2.5 m MAE overall, but larger in steep terrain), the impacts of DEM errors on shortwave radiation in mountains cannot be ignored. Therefore, we declared that the uncertainty of shortwave radiation estimations in mountains largely depends on the accuracy of the DEM dataset at fine spatial resolutions. However, we also found these errors decreased markedly with an increase in spatial scale; thus, it is reliable to use fine-spatial-resolution maps as the bridge to validate coarse-resolution products. Our study emphasizes possible issues in shortwave radiation estimation, which is crucial for energy budget and climate change applications with satellite-derived datasets in mountains.

Code availability

Some codes for DSR and NSR estimation in mountains used in this study are available from http://higlass.whu.edu.cn/tools. For further information, please contact the corresponding author through email.

Declaration of Competing Interest

The authors declare that they have no known competing financial interests or personal relationships that could have appeared to influence the work reported in this paper.

Data Availability

Data will be made available on request.

Acknowledgment

This work was supported by National Key Research and Development Program of China (2020YFA0608704), National Natural Science Foundation of China Grant (42090012), the Hubei Natural Science Foundation Grant (2021CFA082), and the Fundamental Research Funds for the Central Universities through Wuhan University under Grant (2042021kf0203). The data used for this paper have been provided by Landsat of USGS, AW3D30 of the JAXA, and SRTM DEM of NASA Earth Science Data Systems. The in-situ measured data in Chengde was provided by the Chengde Remote Sensing Experimental Station, State Key Laboratory of Remote Sensing Sciences. The authors thank Jiang Chen and Zhili Wang's help in writing the manuscript and Tim McVicar's 'handy hints' for improving it. Finally, we thank three anonymous reviewers for their constructive comments which substantially improved the manuscript.

References

Aguilar, C., Herrero, J., Polo, M.J., 2010. Topographic effects on solar radiation distribution in mountainous watersheds and their influence on reference evapotranspiration estimates at watershed scale. Hydrol. Earth Syst. Sci. 14, 2479–2494.

Amatya, P.M., Ma, Y., Han, C., Wang, B., Devkota, L.P., 2015. Estimation of net radiation flux distribution on the southern slopes of the central Himalayas using MODIS data. Atmos. Res. 154, 146–154.

Belgiu, M., Drăguţ, L., 2016. Random forest in remote sensing: a review of applications and future directions. ISPRS J. Photogramm. Remote Sens. 114, 24–31.

Bian, J., Li, A., Lei, G., Zhang, Z., Nan, X., 2020. Global high-resolution mountain green cover index mapping based on Landsat images and google earth engine. ISPRS J. Photogramm. Remote Sens. 162, 63–76.

Bisht, G., Venturini, V., Islam, S., Jiang, L., 2005. Estimation of the net radiation using MODIS (Moderate resolution imaging spectroradiometer) data for clear sky days. Remote Sens. Environ. 97, 52–67.

Blyth, S., Lysenko, I., Groombridge, B., Miles, L., Newton, A., 2002. Mountain Watch: Environmental Change and Sustainable Development in Mountains. UNEP World Conservation Monitoring Centre, Cambridge, UK.

Bogren, W.S., Burkhart, J.F., Kylling, A., 2016. Tilt error in cryospheric surface radiation measurements at high latitudes: a model study. Cryosphere 10, 613–622.

Carmona, F., Rivas, R., Caselles, V., 2015. Development of a general model to estimate the instantaneous, daily, and daytime net radiation with satellite data on clear-sky days. Remote Sens. Environ. 171, 1–13.

Carrera-Hernández, J.J., 2021. Not all DEMs are equal: An evaluation of six globally available 30 m resolution DEMs with geodetic benchmarks and LiDAR in Mexico. Remote Sens. Environ. 261, 112474.

Chen, J., He, T., Liang, S., 2022. Estimation of daily all-wave surface net radiation with multispectral and multitemporal observations from GOES-16 ABI. IEEE Trans. Geosci. Remote Sens. 60, 1–16.

Chen, L., Yan, G., Wang, T., Ren, H., Calbó, J., Zhao, J., McKenzie, R., 2012. Estimation of surface shortwave radiation components under all sky conditions: modeling and sensitivity analysis. Remote Sens. Environ. 123, 457–469.

Chen, S., Zhang, Y., Wu, Q., Liu, S., Song, C., Xiao, J., Band, L.E., Vose, J.M., 2021. Vegetation structural change and CO2 fertilization more than offset gross primary production decline caused by reduced solar radiation in China. Agric. For. Meteorol. 296, 108207.

Chen, X., Su, Z., Ma, Y., Yang, K., Wang, B., 2013. Estimation of surface energy fluxes under complex terrain of Mt. Qomolangma over the Tibetan Plateau. Hydrol. Earth Syst. Sci. 17, 1607–1618.

Chen, Y., Hall, A., Liou, K.N., 2006. Application of three-dimensional solar radiative transfer to mountains. J. Geophys. Res. 111.

Chu, Q., Yan, G., Qi, J., Mu, X., Li, L., Tong, Y., Zhou, Y., Liu, Y., Xie, D., Wild, M., 2021. Quantitative analysis of terrain reflected solar radiation in snow-covered mountains: a case study in southeastern Tibetan Plateau. J. Geophys. Res. 126, e2020JD034294.

Chu, Q., Yan, G., Wild, M., Zhou, Y., Yan, K., Li, L., Liu, Y., Tong, Y., Mu, X., 2019. Ground-based radiation observational method in mountainous areas. In: 2019 IEEE International Geoscience and Remote Sensing Symposium, pp. 8566–8569.

Dozier, J., Frew, J., 1990. Rapid calculation of terrain parameters for radiation modeling from digital elevation data. IEEE Trans. Geosci. Remote Sens. 28, 963–969.

Garen, D.C., Marks, D., 2005. Spatially distributed energy balance snowmelt modelling in a mountainous river basin: estimation of meteorological inputs and verification of model results. J. Hydrol. 315, 126–153.

Gastellu-Etchegorry, J.P., Martin, E., Gascon, F., 2004. DART: a 3D model for simulating satellite images and studying surface radiation budget. Int. J. Remote Sens. 25, 73–96.

Gottfried, M., Pauli, H., Futschik, A., Akhalkatsi, M., Barančok, P., Benito Alonso, J.L., Coldea, G., Dick, J., Erschbamer, B., Fernández Calzado, M.a.R., Kazakis, G., Krajči, J., Larsson, P., Mallaun, M., Michelsen, O., Moiseev, D., Moiseev, P., Molau, U., Merzouki, A., Nagy, L., Nakhutsrishvili, G., Pedersen, B., Pelino, G., Puscas, M., Rossi, G., Stanisci, A., Theurillat, J.-P., Tomaselli, M., Villar, L., Vittoz, P., Vogiatzakis, I., Grabherr, G., 2012. Continent-wide response of mountain vegetation to climate change. Nat. Clim. Change 2, 111–115.

Guth, P.L., Van Niekerk, A., Grohmann, C.H., Muller, J.-P., Hawker, L., Florinsky, I.V., Gesch, D., Reuter, H.I., Herrera-Cruz, V., Riazanoff, S., López-Vázquez, C., Carabajal, C.C., Albinet, C., Strobl, P., 2021. Digital elevation models: terminology and definitions. Remote Sens. 13, 3581.

Hansen, L.B., Kamstrup, N., Hansen, B.U., 2002. Estimation of net short-wave radiation by the use of remote sensing and a digital elevation model-a case study of a high arctic mountainous area. Int. J. Remote Sens. 23, 4699–4718.

Hao, D., Bisht, G., Gu, Y., Lee, W.L., Liou, K.N., Leung, L.R., 2021. A parameterization of sub-grid topographical effects on solar radiation in the E3SM Land Model (version 1.0): implementation and evaluation over the Tibetan Plateau. Geosci. Model. Dev. 14, 6273–6289.

Hao, D., Wen, J., Xiao, Q., Lin, X., You, D., Tang, Y., Liu, Q., Zhang, S., 2019a. Sensitivity of coarse-scale snow-free land surface shortwave albedo to topography. J. Geophys. Res. 124, 9028–9045.

Hao, D., Wen, J., Xiao, Q., Wu, S., Lin, X., You, D., Tang, Y., 2019b. Impacts of DEM geolocation bias on downward surface shortwave radiation estimation over clear-sky rugged terrain: a case study in Dayekou Basin, China. IEEE Geosci. Remote Sens. Lett. 16, 10–14.

He, T., Liang, S., Wang, D., Cao, Y., Gao, F., Yu, Y., Feng, M., 2018a. Evaluating land surface albedo estimation from Landsat MSS, TM, ETM+, and OLI data based on the unified direct estimation approach. Remote Sens. Environ. 204, 181–196.

He, T., Liang, S., Wang, D., Shi, Q., Goulden, M.L., 2015. Estimation of high-resolution land surface net shortwave radiation from AVIRIS data: algorithm development and preliminary results. Remote Sens. Environ. 167, 20–30.

He, T., Liang, S., Wang, D., Shi, Q., Tao, X., 2014. Estimation of high-resolution land surface shortwave albedo from AVIRIS data. IEEE J. Sel. Top. Appl. Earth Obs. Remote Sens. 7, 4919–4928.

He, Z., Du, J., Chen, L., Zhu, X., Lin, P., Zhao, M., Fang, S., 2018b. Impacts of recent climate extremes on spring phenology in arid-mountain ecosystems in China. Agric. For. Meteorol. 260-261, 31–40.

Helbig, N., L'we, H., Mayer, B., Lehning, M., 2010. Explicit validation of a surface shortwave radiation balance model over snow-covered complex terrain. J. Geophys. Res. 115, D18113.
Helbig, N., Löwe, H., 2012. Shortwave radiation parameterization scheme for subgrid topography. J. Geophys. Res. 117, D03112.
Horn, B.K.P., 1981. Hill shading and the reflectance map. Proc. IEEE 69, 14–47.
Huang, G., Li, Z., Li, X., Liang, S., Yang, K., Wang, D., Zhang, Y., 2019. Estimating surface solar irradiance from satellites: past, present, and future perspectives. Remote Sens. Environ. 233, 111371.
Huang, J., Yu, H., Guan, X., Wang, G., Guo, R., 2016. Accelerated dryland expansion under climate change. Nat. Clim. Change 6, 166–171.
Huang, P., Zhao, W., Li, A., 2017. The preliminary investigation on the uncertainties associated with surface solar radiation estimation in mountainous areas. IEEE Geosci. Remote Sens. Lett. 14, 1071–1075.
Immerzeel, W.W., Lutz, A.F., Andrade, M., Bahl, A., Biemans, H., Bolch, T., Hyde, S., Brumby, S., Davies, B.J., Elmore, A.C., Emmer, A., Feng, M., Fernández, A., Haritashya, U., Kargel, J.S., Koppes, M., Kraaijenbrink, P.D.A., Kulkarni, A.V., Mayewski, P.A., Nepal, S., Pacheco, P., Painter, T.H., Pellicciotti, F., Rajaram, H., Rupper, S., Sinisalo, A., Shrestha, A.B., Viviroli, D., Wada, Y., Xiao, C., Yao, T., Baillie, J.E.M., 2020. Importance and vulnerability of the world's water towers. Nature 577, 364–369.
Jenness, J.S., 2004. Calculating landscape surface area from digital elevation models, 32. Wildlife Society Bulletin, pp. 829–839.
Jing, C., Shortridge, A., Lin, S., Wu, J., 2014. Comparison and validation of SRTM and ASTER GDEM for a subtropical landscape in Southeastern China. Int. J. Digital Earth 7, 969–992.
Jones, K.H., 1998. A comparison of algorithms used to compute hill slope as a property of the DEM. Comput. Geosci. 24, 315–323.
JPL, N. (2013). NASA Shuttle Radar Topography Mission Global 1 arc second. In N.E.L.P. DAAC (Ed.).
Lai, Y.-J., Chou, M.-D., Lin, P.-H., 2010. Parameterization of topographic effect on surface solar radiation. J. Geophys. Res. 115, D01104.
Lee, W.-L., Liou, K.N., Wang, C.-c, 2013. Impact of 3-D topography on surface radiation budget over the Tibetan Plateau. Theor. Appl. Climatol. 113, 95–103.
Letu, H., Shi, J., Li, M., Wang, T., Shang, H., Lei, Y., Ji, D., Wen, J., Yang, K., Chen, L., 2020. A review of the estimation of downward surface shortwave radiation based on satellite data: Methods, progress and problems. Sci. China Earth Sci. 63, 774–789.
Li, G., Li, Y., Lin, H., Ye, Q., Jiang, L., 2021. Two periods of geodetic glacier mass balance at Eastern Nyainqentanglha derived from multi-platform bistatic SAR interferometry. Int. J. Appl. Earth Obs. Geoinf. 104, 102541.
Li, X., Toshio, K., Cheng, G., 2002. Retrieval of snow reflectance from Landsat data in rugged terrain. Ann. Glaciol. 34, 31–37.
Liang, S., 2001. Narrowband to broadband conversions of land surface albedo I: Algorithms. Remote Sens. Environ. 76, 213–238.
Liang, S., Wang, D., He, T., Yu, Y., 2019. Remote sensing of earth's energy budget: synthesis and review. Int. J. Digital Earth 12, 737–780.
Liu, K., Song, C., Ke, L., Jiang, L., Pan, Y., Ma, R., 2019. Global open-access DEM performances in Earth's most rugged region High Mountain Asia: a multi-level assessment. Geomorphology 338, 16–26.
Long, D., Gao, Y., Singh, V.P., 2010. Estimation of daily average net radiation from MODIS data and DEM over the Baiyangdian watershed in North China for clear sky days. J. Hydrol. 388, 217–233.
Lu, J., He, T., Liang, S., Zhang, Y., 2022. An automatic radiometric cross-calibration method for wide-angle medium-resolution multispectral satellite sensor using Landsat data. IEEE Trans. Geosci. Remote Sens. 60, 1–11.
Lyapustin, A., & Wang, Y. (2018). MCD19A2 MODIS/Terra+Aqua Land Aerosol Optical Depth Daily L2G Global 1km SIN Grid V006. In N.E.L.P. DAAC (Ed.).
Ma, Y., He, T., Li, A., Li, S., 2021. Evaluation and intercomparison of topographic correction methods based on landsat images and simulated data. Remote Sens. 13, 4120.
Ma, Y., He, T., Liang, S., Wen, J., Gastellu-Etchegorry, J.P., Chen, J., Ding, A., Feng, S., 2022. Landsat snow-free surface albedo estimation over sloping terrain: algorithm development and evaluation. IEEE Trans. Geosci. Remote Sens. 60, 1–14.
Martins, V.S., Lyapustin, A., de Carvalho, L.A.S., Barbosa, C.C.F., Novo, E.M.L.M., 2017. Validation of high-resolution MAIAC aerosol product over South America. J. Geophys. Res. 122, 7537–7559.
Martins, V.S., Lyapustin, A., Wang, Y., Giles, D.M., Smirnov, A., Slutsker, I., Korkin, S., 2019. Global validation of columnar water vapor derived from EOS MODIS-MAIAC algorithm against the ground-based AERONET observations. Atmos. Res. 225, 181–192.
Mira, M., Olioso, A., Gallego-Elvira, B., Courault, D., Garrigues, S., Marloie, O., Hagolle, O., Guillevic, P., Boulet, G., 2016. Uncertainty assessment of surface net radiation derived from Landsat images. Remote Sens. Environ. 175, 251–270.
Nyman, P., Baillie, C.C., Duff, T.J., Sheridan, G.J., 2018. Eco-hydrological controls on microclimate and surface fuel evaporation in complex terrain. Agric. For. Meteorol. 252, 49–61.
Olson, M., Rupper, S., Shean, D.E., 2019. Terrain induced biases in clear-sky shortwave radiation due to digital elevation model resolution for glaciers in complex terrain. New Front. Rare Earth Sci. Appl., Proc. Int. Conf. Rare Earth Dev. Appl. 7.
Pepin, N., Bradley, R.S., Diaz, H.F., Baraer, M., Caceres, E.B., Forsythe, N., Fowler, H., Greenwood, G., Hashmi, M.Z., Liu, X.D., Miller, J.R., Ning, L., Ohmura, A., Palazzi, E., Rangwala, I., Schöner, W., Severskiy, I., Shahgedanova, M., Wang, M.B., Williamson, S.N., Yang, D.Q., Mountain Research Initiative, E.D.W.W.G, 2015. Elevation-dependent warming in mountain regions of the world. Nat. Clim. Change 5, 424–430.
Sandmeier, S., Itten, K.I., 1997. A physically-based model to correct atmospheric and illumination effects in optical satellite data of rugged terrain. IEEE Trans. Geosci. Remote Sens. 35, 708–717.
Shi, H., Xiao, Z., 2021. Exploring topographic effects on surface parameters over rugged terrains at various spatial scales. IEEE Trans. Geosci. Remote Sens. 60, 1–16.
Shi, Q., Liang, S., 2013. Characterizing the surface radiation budget over the Tibetan Plateau with ground-measured, reanalysis, and remote sensing data sets: 1. Methodology. J. Geophys. Res. 118, 9642–9657.
Storey, J., Choate, M., Lee, K., 2014. Landsat 8 operational land imager on-orbit geometric calibration and performance. Remote Sens. 6, 11127–11152.
Superczynski, S.D., Kondragunta, S., Lyapustin, A.I., 2017. Evaluation of the multi-angle implementation of atmospheric correction (MAIAC) aerosol algorithm through intercomparison with VIIRS aerosol products and AERONET. J. Geophys. Res. 122, 3005–3022.
Tadono, T., Ishida, H., Oda, F., Naito, S., Minakawa, K., Iwamoto, H., 2014. Precise global DEM generation by ALOS PRISM. ISPRS Ann. Photogramm. Remote Sens. Spatial Inf. Sci. 71–76. *II-4*.
Tan, M.L., Ficklin, D.L., Dixon, B., Ibrahim, A.L., Yusop, Z., Chaplot, V., 2015. Impacts of DEM resolution, source, and resampling technique on SWAT-simulated streamflow. Appl. Geogr. 63, 357–368.
Vaze, J., Teng, J., Spencer, G., 2010. Impact of DEM accuracy and resolution on topographic indices. Environ. Model. Softw. 25, 1086–1098.
Vermote, E.F., Tanre, D., Deuze, J.L., Herman, M., Morcette, J., 1997. Second simulation of the satellite signal in the solar spectrum, 6S: an overview. IEEE Trans. Geosci. Remote Sens. 35, 675–686.
Wang, D., Liang, S., He, T., Shi, Q., 2015. Estimation of daily surface shortwave net radiation from the combined MODIS Data. IEEE Trans. Geosci. Remote Sens. 53, 5519–5529.
Wang, D., Liang, S., Li, R., Jia, A., 2021. A synergic study on estimating surface downward shortwave radiation from satellite data. Remote Sens. Environ. 264, 112639.
Wang, L., Wang, K., 2015. Impacts of DEM uncertainty on estimated surface solar radiation and extracted river network. Bull. Am. Meteorol. Soc. 96, 297–304.
Wang, T., Yan, G., Mu, X., Jiao, Z., Chen, L., Chu, Q., 2018. Toward operational shortwave radiation modeling and retrieval over rugged terrain. Remote Sens. Environ. 205, 419–433.
Wang, Y., Lauret, N., Gastellu-Etchegorry, J.-P., 2020. DART radiative transfer modelling for sloping landscapes. Remote Sens. Environ. 247, 111902.
Wen, J., You, D., Han, Y., Lin, X., Wu, S., Tang, Y., Xiao, Q., Liu, Q., 2022. Estimating surface BRDF/Albedo over rugged terrain using an Extended Multisensor Combined BRDF Inversion (EMCBI) model. IEEE Geosci. Remote Sens. Lett. 19, 1–5.
Wild, M., Folini, D., Schär, C., Loeb, N., Dutton, E.G., König-Langlo, G., 2013. The global energy balance from a surface perspective. Clim. Dyn. 40, 3107–3134.
Woodcock, C.E., Allen, R., Anderson, M., Belward, A., Bindschadler, R., Cohen, W., Gao, F., Goward, S.N., Helder, D., Helmer, E., Nemani, R., Oreopoulos, L., Schott, J., Thenkabail, P.S., Vermote, E.F., Vogelmann, J., Wulder, M.A., Wynne, R., 2008. Free access to landsat imagery. Science 320, 1011.
Wu, J., Su, Y., Chen, X., Liu, L., Yang, X., Gong, F., Zhang, H., Xiong, X., Zhang, D., 2021. Leaf shedding of Pan-Asian tropical evergreen forests depends on the synchrony of seasonal variations of rainfall and incoming solar radiation. Agric. For. Meteorol. 311, 108691.
Wu, S., Wen, J., You, D., Hao, D., Lin, X., Xiao, Q., Liu, Q., Gastellu-Etchegorry, J.-P., 2018. Characterization of remote sensing albedo over sloped surfaces based on DART simulations and in situ observations. J. Geophys. Res. 123, 8599–8622.
Wu, X., Wen, J., Xiao, Q., Bao, Y., You, D., Wang, J., Ma, D., Lin, X., Gong, B., 2022. Quantification of the uncertainty caused by geometric registration errors in multiscale validation of satellite products. IEEE Geosci. Remote Sens. Lett. 19, 1–5.
Wulder, M.A., Loveland, T.R., Roy, D.P., Crawford, C.J., Masek, J.G., Woodcock, C.E., Allen, R.G., Anderson, M.C., Belward, A.S., Cohen, W.B., Dwyer, J., Erb, A., Gao, F., Griffiths, P., Helder, D., Hermosilla, T., Hipple, J.D., Hostert, P., Hughes, M.J., Huntington, J., Johnson, D.M., Kennedy, R., Kilic, A., Li, Z., Lymburner, L., McCorkel, J., Pahlevan, N., Scambos, T.A., Schaaf, C., Schott, J.R., Sheng, Y., Storey, J., Vermote, E., Vogelmann, J., White, J.C., Wynne, R.H., Zhu, Z., 2019. Current status of Landsat program, science, and applications. Remote Sens. Environ. 225, 127–147.
Xiao, X., Zhang, T., Zhong, X., Li, X., 2020. Spatiotemporal Variation of Snow Depth in the Northern Hemisphere from 1992 to 2016. Remote Sens. 12, 2728.
Xie, X., Li, A., 2020. Development of a topographic-corrected temperature and greenness model (TG) for improving GPP estimation over mountainous areas. Agric. For. Meteorol. 295, 108193.
Xu, L., Long, E., Wei, J., Cheng, Z., Zheng, H., 2021. A new approach to determine the optimum tilt angle and orientation of solar collectors in mountainous areas with high altitude. Energy 237, 121507.
Xu, S., Yu, Z., Lettenmaier, D.P., McVicar, T.R., Ji, X., 2020. Elevation-dependent response of vegetation dynamics to climate change in a cold mountainous region. Environ. Res. Lett. 15, 094005.
Yan, G., Chu, Q., Tong, Y., Mu, X., Qi, J., Zhou, Y., Liu, Y., Wang, T., Xie, D., Zhang, W., Yan, K., Chen, S., Zhou, H., 2021. An operational method for validating the downward shortwave radiation over rugged terrains. IEEE Trans. Geosci. Remote Sens. 59, 714–731.
Yan, G., Jiao, Z.-H., Wang, T., Mu, X., 2020. Modeling surface longwave radiation over high-relief terrain. Remote Sens. Environ. 237, 111556.
Yan, G., Tong, Y., Yan, K., Mu, X., Chu, Q., Zhou, Y., Liu, Y., Qi, J., Li, L., Zeng, Y., Zhou, H., Xie, D., Zhang, W., 2018. Temporal extrapolation of daily downward shortwave radiation over cloud-free rugged terrains. Part 1: analysis of topographic effects. IEEE Trans. Geosci. Remote Sens. 56, 6375–6394.

Yan, G., Wang, T., Jiao, Z., Mu, X., Zhao, J., Chen, L., 2016. Topographic radiation modeling and spatial scaling of clear-sky land surface longwave radiation over rugged terrain. Remote Sens. Environ. 172, 15–27.
Yang, K., Pinker, R.T., Ma, Y., Koike, T., Wonsick, M.M., Cox, S.J., Zhang, Y., Stackhouse, P., 2008. Evaluation of satellite estimates of downward shortwave radiation over the Tibetan Plateau. J. Geophys. Res. 113.
Zapadka, T., Ostrowska, M., Stoltmann, D., Krężel, A., 2020. A satellite system for monitoring the radiation budget at the Baltic Sea surface. Remote Sens. Environ. 240, 111683.
Zhan, P., Song, C., Luo, S., Liu, K., Ke, L., Chen, T., 2021. Lake level reconstructed from DEM-based virtual station: comparison of multisource DEMs with laser altimetry and UAV-LiDAR measurements. IEEE Geosci. Remote Sens. Lett. 1–5.
Zhang, S., Li, X., She, J., Peng, X., 2019. Assimilating remote sensing data into GIS-based all sky solar radiation modeling for mountain terrain. Remote Sens. Environ. 231, 111239.
Zhang, X., Liang, S., Zhou, G., Wu, H., Zhao, X., 2014. Generating global land surface satellite incident shortwave radiation and photosynthetically active radiation products from multiple satellite data. Remote Sens. Environ. 152, 318–332.
Zhang, Y., Li, X., Bai, Y., 2015. An integrated approach to estimate shortwave solar radiation on clear-sky days in rugged terrain using MODIS atmospheric products. Sol. Energy 113, 347–357.
Zhang, Y.L., Li, X., Cheng, G.D., Jin, H.J., Yang, D.W., Flerchinger, G.N., Chang, X.L., Wang, X., Liang, J., 2018. Influences of topographic shadows on the thermal and hydrological processes in a cold region mountainous watershed in northwest China. J. Adv. Model Earth Syst. 10, 1439–1457.
Zhao, W., Yang, M., Chang, R., Zhan, Q., Li, Z.-L., 2021. Surface warming trend analysis based on MODIS/Terra land surface temperature product at Gongga Mountain in the southeastern Tibetan Plateau. J. Geophys. Res. 126, e2020JD034205.